

Bouncing behaviour of a particle settling through a density transition layer

Shuhong Wang¹, Prabal Kandel¹, Jian Deng^{1†}, C.P. Caulfield² and Stuart B. Dalziel²

¹State Key Laboratory of Fluid Power and Mechatronic Systems, Department of Mechanics, Zhejiang University, Hangzhou 310027, People's Republic of China.

²Department of Applied Mathematics & Theoretical Physics, University of Cambridge, Cambridge CB3 0WA, UK

(Received xx; revised xx; accepted xx)

The present work focuses on a specific bouncing behaviour as a particle settling through a three-layer stratified fluid in the absence of neutral buoyant position, which was firstly discovered by [Abaid & McLaughlin \(2004\)](#) in salinity-induced stratification. Both experiments and numerical simulations are carried out. In our experiments, illuminated by a laser sheet on the central plane of the particle, its bouncing behaviour is well captured. We find that the bouncing process starts after the wake detaches from the particle. The PIV results show that an upward jet is generated at the central axis behind the particle after the wake breaks. By conducting a force decomposition procedure, we quantify the enhanced drag caused by the buoyancy of the wake (F_{sb}) and the flow structure (F_{sj}). It is noted that F_{sb} contributes primarily to the enhanced drag at the early stage, which becomes less dominant after the detachment of the wake. In contrast, F_{sj} plays a pivotal role in reversing the particle's motion. We conjecture that the jet flow is a necessary condition for the occurrence of bouncing motion. Then, we examine the minimal velocities (negative values when bounce occurs) of the particle by varying the lower Reynolds number Re_l , the Froude number Fr and the upper Reynolds number Re_u within the ranges $1 \leq Re_l \leq 125$, $115 \leq Re_u \leq 356$ and $2 \leq Fr \leq 7$. We find that the bouncing behaviour is primarily determined by Re_l . In our experiments, the bouncing motion is found to occur below a critical lower Reynolds number around $Re_l^* = 30$. In the numerical simulations, the highest value for this critical number is $Re_l^* = 46.2$, limited in the currently studied parametric ranges.

Key words: stratified fluid, settling particle, bouncing behaviour, jet flow

1. Introduction

Density stratification caused by nonuniform distributions of temperature or salinity is ubiquitous in oceans and lakes, which alters the settling or rising process of submerging particles, and has marked effects on many environmental problems, such as the aggregation of marine snow, the formation of thin layers, the dispersion of spilling oil and the deposition of sediments ([Prairie & White 2017](#); [Diercks & Montoya 2019](#)). Understanding the fluid dynamics of particle settling (or rising) in a stratified ambient fluid is of considerable significance for better predictions of those actions.

† Email address for correspondence: zjudengjian@zju.edu.cn

In homogeneous fluid, the hydrodynamic force acting on a particle accelerating under gravity can be decomposed into buoyancy force, steady-state drag, added mass, and history (Basset) force. The steady-state drag increases with velocity and finally balances the reduced gravity, such that the particle reaches a steady state. In stratified fluid, the particle experiences an additional drag force due to the stratification, noted as ‘stratification drag’, yielding a significant decay in settling velocity (Srdić-Mitrović & Fernando 1999; Abaid & McLaughlin 2004; Camassa & Parker 2009; Yick *et al.* 2009; Camassa & Mykins 2010; Doostmohammadi & Ardekani 2014b; Verso & Liberzon 2019; Mandel & Khatri 2020; Magnaudet & Mercier 2020).

There have been different explanations for the origin of stratification drag. A widely accepted one is that it comes from the buoyancy of associated upper lighter fluid, as the settling particle distorts the isopycnals and drags some upper fluid to a lower position. Srdić-Mitrović & Fernando (1999) conducted experiments of particles settling in a three-layer stratified fluid, with two homogeneous layers and one density transition layer (interface) in between, at Reynolds numbers $1.5 \leq Re \leq 15$ and Froude numbers $3 \leq Fr \leq 10$. They found that the total drag enhancement can be estimated by the total buoyancy of the upper fluid dragged below the upper bound of the interface, before the maximum drag is reached. The contribution of internal waves is negligible before the wake breaks as they are generated after the rupture of the wake. With the same type of stratification, Verso & Liberzon (2019) studied experimentally the motion of four different particles, in a wider parameter range ($2 \leq Re \leq 106$ and $0.5 \leq Fr \leq 28$). A time-dependent stratification force model was developed for those particles, based on the assumption that the stratification force is entirely contributed by the buoyancy of an effective wake, and the wake volume is constant within the interface and decreases exponentially till a new terminal velocity is reached.

In a linearly stratified fluid, a combined experimental and numerical investigation of settling particles at small Reynolds numbers ($Re \sim O(1)$) was presented by Yick *et al.* (2009). They found that the buoyancy of a shell of fluid around the particle, instead of the entire distorted region, is responsible for the drag enhancement. Furthermore, they suggested that the total drag increment can be scaled by a dimensionless parameter, the Richardson number, characterising the relative importance of buoyancy and viscous shear force. A similar mechanism was also found for the stratification drag of a rising grid of bars (Higginson & Linden 2003), at much higher Reynolds numbers ($Re \sim O(10^3)$), using the drift volume as an approximation of the volume of dragged fluid.

Although the associated buoyancy accounts for the stratification drag in many cases, Zhang & Magnaudet (2019) pointed out that it is the specific structure of the vorticity field induced by the buoyancy effects that contributes mainly to the stratification drag, while the buoyancy itself plays a secondary role. Moreover, Torres *et al.* (2000) noted that the drag enhancement is rather small until a vertical upward jet is generated at the rear of the particle at relatively strong stratification ($Fr \lesssim 20$), evidencing the drag contribution from the flow structure.

The flow structure manifested by the vertical motion of a particle in a stratified fluid is notably different from that in a homogeneous fluid. In a stratified fluid, the baroclinic torque ($\nabla\rho \times \nabla p$) results in vorticity generation whenever there is a misalignment between density and pressure gradient (Magnaudet & Mercier 2020). For low Reynolds numbers ($Re \ll 1$), top-down symmetrical toroidal eddies are induced by a vertical, downward point force (Stokeslet) under linear stratification, which is similar to the eddy formed under the restriction of two horizontal walls, indicating the suppression of vertical flow by stratification (Ardekani & Stocker 2010). For higher Reynolds numbers ($0.05 \leq Re \leq 100$), toroidal eddies still exist but lose the top-down symmetry, and a

vertical upward jet is generated simultaneously at the centre line downstream of the particle (Zhang & Magnaudet 2019). This jet was experimentally observed over a wide range of Froude numbers, $0.2 \leq Fr \leq 70$, and Reynolds numbers, $30 \leq Re \leq 4000$, with its shape and strength varying with Re and Fr (Hanazaki & Okamura 2009).

The present work focuses on the transient bouncing behaviour as a particle passes through a density transition layer with a large density gradient, while the particle density is always higher than the fluid such that no neutral position exists. This phenomenon was first observed by Abaid & McLaughlin (2004) in their experiments with a strong salt stratification. As we know that in continuous concentration-induced stratified fluid, a droplet could bounce and oscillate under the Maragoni effects induced by nonuniform surface tension (Blanchette & Shapiro 2012; Li & Lohse 2019). However, this mechanism could not be applied to a solid particle, as surface tension does not exist at a solid-liquid surface. Abaid & McLaughlin (2004) observed that before the particle bounces up, the entrained plume detaches and ascends to the upper layer, which indicates that the particle is possibly lifted by the plume. However, the detached plume moving opposite to the particle is not uniquely associated with the bouncing behaviour. A descending wake of a droplet rising through a density interface could not trigger a reverse motion (Mandel & Khatri 2020). Moreover, wake rupture was also observed experimentally for a descending solid particle (Srđić-Mitrović & Fernando 1999). Therefore it is of interest to further explore the mechanisms accounting for the bouncing of a solid particle.

As the bouncing behaviour occurs at certain combinations of parameters, a parametric study is necessary, before we further investigate the bouncing mechanisms. Previous work revealed that the bouncing behaviour is affected by a variety of parameters. Camassa & Vaidya (2022) found that the critical particle density ρ_p for the occurrence of bouncing can be expressed by a linear combination of upper and lower layer fluid densities. Doostmohammadi & Ardekani (2014a) found that at a relatively higher density ratio of $(\rho_l - \rho_u)/\rho_u$, an ellipsoid could bounce for a short time as it passes through a density interface. Additionally, Blanchette & Shapiro (2012) found that high ratio of $(\rho_p - \rho_u)/(\rho_p - \rho_l)$ could lead to a temporary reverse motion of a drop as it settles through a density transition layer with identical surface tension. These studies indicate that the bouncing behaviour is strongly dependent on the density or density ratio of the system. Moreover, the Froude number is a key parameter affecting the oscillation of a particle or droplet near their neutral buoyant position in a linear stratified fluid (Bayareh & Ardekani 2013; Doostmohammadi & Ardekani 2014b). In the experiments carried out by Abaid & McLaughlin (2004), the transient levitation of the particles was discovered by adjusting the lower terminal velocities, which means that the lower Reynolds number should be taken into account. As we know, in three-layer stratification, both the Froude number and the Reynolds number are dependent on the density difference. Whether the controlling parameter of the bouncing motion is the density difference, or other relevant parameters, is necessary to be addressed.

The paper is organised as follows: In section 2, we introduce the experimental method, including experimental setup and measurement. The numerical method and validation are presented in section 3. We discuss our results in section 4. We present the settling process of a typical bouncing particle, and analyse the forces acting on it, to understand the mechanisms of bouncing behaviour. Then we examine the effects of Re_l , Fr and Re_u on the minimal velocity of the particle, to identify the key controlling parameter. Conclusions are drawn in section 5.

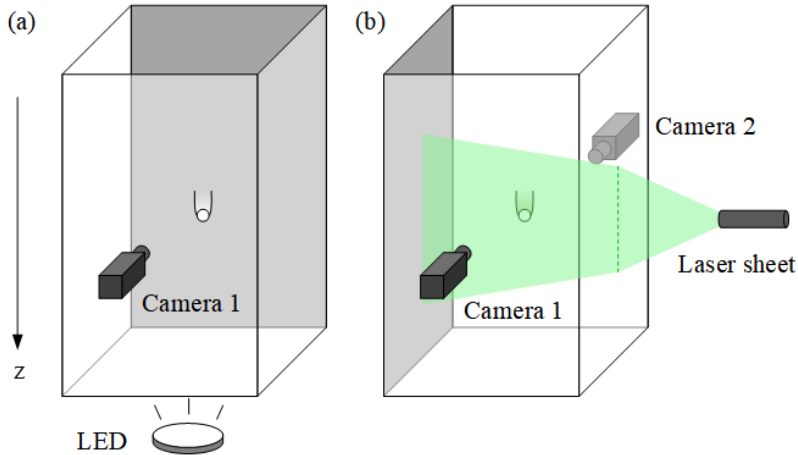


FIGURE 1. Experimental setups. (a) Setup 1 for recording particles trajectories; (b) Setup 2 for wake visualisation and flow fields measurement.

2. Experimental approach

2.1. Experimental setup

The experiments were performed in a glass tank, with a total depth of 60 cm to ensure that terminal velocity was achieved. The tank has a large base area (30 cm \times 30 cm) to avoid interaction between the particle and the tank walls. To prepare the working fluids, salt is dissolved in fresh water with different concentration ratios in several separate buckets. They are then kept at room temperature for at least 24 hours before filling the tank, to eliminate resolved gas and get uniformly stable concentration distribution.

The tank is first half-filled by heavy fluid. Then light fluid is pumped slowly and horizontally to the top of the heavy fluid by a micropump, at a low flow rate of 100 ml/min, to minimise mixing of the two fluids. This filling method yields an error-function-type density profile. The tank is let stand for at least half an hour after the filling, and before the experiments, to diminish the disturbances caused by the pumping. The standing time varies with cases to get different thickness of the transition layer, i.e., thicker transition layer needs longer time for the interdiffusion of two fluids.

Nylon particles are used for the experiments, with diameter $D = 10$ mm and densities ranging from 1121-1126 kg/cm³. The particles are released by a fixed clamp, at the centre of the tank cross-section (15 cm from the side walls), 2 cm below the free surface, and approximately 25 cm above the density transition layer. The particles are retained in another tank of stratified fluid at the same room temperature before release. Particle density measurements are conducted just before the experiments. The time interval between each release is 10 minutes, ensuring that the fluid is relaxed to its quiescent state. The settling processes of particles are captured by a high speed camera at a frame rate of 100 fps.

Two different experimental setups are used, as shown in figure 1, to meet the requirements respectively for recording the trajectories of particles, and measuring the surrounding flow fields. For trajectory recording, we simply position a single camera at one side of the tank, and illuminate the tank via a panel of light emitting diodes (LEDs) from the bottom (figure 1(a)). The opposite sidewall of the tank is brushed black paint to avoid light reflection. The size of camera captured window is about 20 \times 20 cm, yielding a resolution of 0.2 mm/pixel.

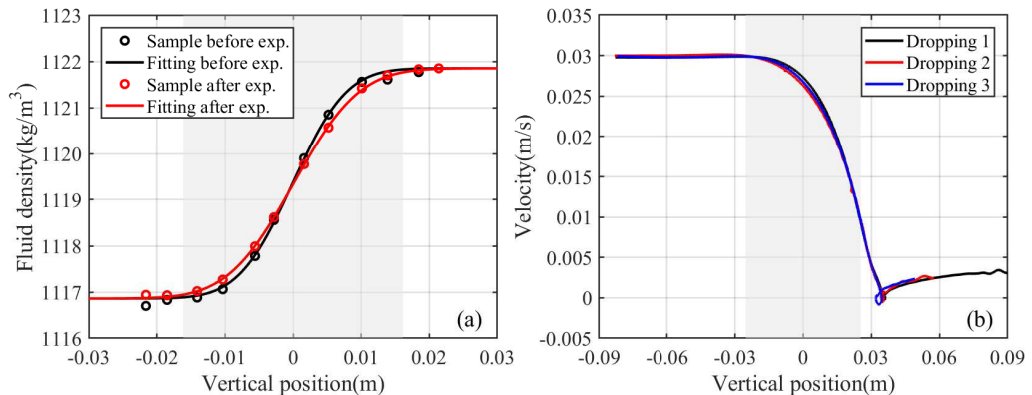


FIGURE 2. (a) Density distribution before and after one experiment. The grey area represents the density interface, which covers 98% density variation between the upper and lower layers. (b) Velocity profiles of three repeated droppings of a same particle.

In the second experimental setup, the upper fluid is dyed using Rhodamine B for wake visualisation, and seeding particles are added to both the upper and lower layer fluids for Particle Image Velocimetry (PIV) measurement. To simultaneously capture the visualised wake structure and measure the velocity fields, two cameras are placed at opposite sides of the tank and carefully adjusted to get their optical axis parallel (figure 1(b)). The centre plane of the tank which is perpendicular to the camera optical axis is illuminated by a laser sheet (thickness ~ 2 mm) sideways. The two cameras are synchronised to obtain simultaneous image pairs. One camera is equipped with a long-pass filter to capture the dyed wake, and the other one with short-pass filter to get the images of seeding particles. To capture the flow structure of the whole settling process, the particle should stay within the illuminated laser sheet plane. The densities of the particle and fluid should be carefully chosen to avoid out-of-plane motion, and the particle should be released very carefully to minimise disturbances. It is worth mentioning that the laser sheet hits the particle surface and heats the vicinity fluid. This effect is negligible in the upper layer as the particle settles fast but prolongs the suspending time after it enters the lower layer. For flow visualisation and PIV measurements, where we focus on the flow structure, the laser sheet is still an effective illumination approach.

2.2. Experimental measurements

The fluid density is measured by a densitometer (Anton-Parr DMA 4500) with measuring accuracy of 0.01 kg/m^3 . To measure the particle density with the same accuracy, the particle is suspended in a tank ($10 \times 10 \times 50 \text{ cm}$) filled with the fluid of an approximately linear density profile. The sampled fluid at the same level of the suspended particle is then measured, of which the density is taken as the particle density. Particle diameters are measured by a micrometer with accuracy of 0.001 mm .

To measure the density distribution of the transition layer, 12 thin needles are inserted horizontally into the tank from punched holes at the sidewall, with 4 mm vertical intervals, and connected to 12 syringes for taking samples. Each sample takes 2.5 ml fluid. For each measurement, 30 ml fluid is taken in total, which leads to a variation in height of less than 0.4 mm , for the working tank of cross-section $30 \text{ cm} \times 30 \text{ cm}$. Thus the modification to the density distribution by the measurement can be ignored. Density distribution measurements are performed twice for each test, before and after dropping the particles, respectively.

The measured density of the 12 samples are fitted to an error-function-shaped function, satisfying the following expression:

$$\rho = \frac{\rho_u + \rho_l}{2} + \frac{\rho_u - \rho_l}{2} \text{erf}(\alpha(h - h_{ref})), \quad (2.1)$$

where ρ_u and ρ_l are respectively the upper and lower layer fluid densities, h_{ref} is the reference height, corresponding to the centre of the density transition layer, α is a scaling factor, determining the thickness of the density transition layer, and $\text{erf}(x)$ is the error function, which is written as

$$\text{erf}(x) = \frac{2}{\pi} \int_0^x e^{-t^2} dt. \quad (2.2)$$

The measured density profiles for one of the experiments are presented in figure 2(a). We can see that the density profile becomes smoother after the experiment. The average of these two measurements is then used as the final density profile.

It is important to monitor and control the temperature of working fluid. With a salinity of 16% and temperature of 18°C (according to the present working fluid), 1°C of temperature variation can lead to 0.41 g/cm³ density variation of the fluid. The natural room temperature variation from daytime to nighttime can be up to 10°C, which may significantly alter the particle behaviour. To minimise the temperature variation of the working fluid, the experiments are conducted in an enclosed room with the room temperature controlled by an air conditioner. The real-time temperature is monitored during each test, and the temperature variation for all tests is maintained at less than 1°C. The density measurement for each particle is conducted just before the dropping to minimise the influence of temperature.

The viscosity of fluid is calculated by the following empirical formula with accuracy of $\pm 1.5\%$ (see equation 22 in the reference by [Sharqawy & Zubair \(2010\)](#)):

$$\begin{cases} \mu = \mu_w(1 + a_1 S_a + a_2 S_a^2), \\ \mu_w = 4.2844 \times 10^{-5} + 0.157(T_e + 64.993)^2 - 91.296)^{-1}, \\ a_1 = 1.541 + 1.998 \times 10^{-2} T_e - 9.52 \times 10^{-5} T_e^2, \\ a_2 = 7.974 - 7.561 \times 10^{-2} T_e + 4.724 \times 10^{-4} T_e^2, \end{cases} \quad (2.3)$$

where S_a and T_e are salinity and temperature respectively.

Instantaneous particle displacements are obtained by fitting the discrete time-dependent position points with a cubic smoothing spline, following the methods of [Truscott & Techet \(2012\)](#) and [Epps \(2010\)](#). The fitting error tolerance is $E=1e-7$ for all experimental position data, which provides accurate fitting data and gives smooth fitting derivatives. Then, the velocity and acceleration of the particles can be calculated based on the time histories of the fitted particle displacements.

Since the passing of particles will introduce disturbances to the density transition layer and expedite the diffusion, no more than five particles are dropped in each fluid tank. The repeatability validation is conducted separately before the experiment. As presented in figure 2(b), the settling dynamics is almost unchanged for the repeated releases.

3. Numerical method

We solve the time-dependent incompressible Navier-Stokes equations with finite volume method. The continuity and the momentum equations are expressed as

$$\nabla \cdot \mathbf{u} = 0, \quad (3.1)$$

$$\rho \left(\frac{\partial \mathbf{u}}{\partial t} + \mathbf{u} \cdot \nabla \mathbf{u} \right) = -\nabla p + \mu \nabla^2 \mathbf{u} + \rho \mathbf{g}. \quad (3.2)$$

The Boussinesq approximation is applied to account for the stratification effect, where the density variation enters the momentum equation only through the buoyancy term. Division by the reference density in (3.2) yields

$$\frac{\partial \mathbf{u}}{\partial t} + \mathbf{u} \cdot \nabla \mathbf{u} = -\frac{1}{\rho_{ref}} \nabla p + \frac{\rho}{\rho_{ref}} \mathbf{g} + \nu \nabla^2 \mathbf{u}, \quad (3.3)$$

with kinematic viscosity $\nu = \mu/\rho_{ref}$. The transport equation for density is given as

$$\frac{\partial \rho}{\partial t} + \mathbf{u} \cdot \nabla \rho = \kappa \nabla^2 \rho, \quad (3.4)$$

where κ is the scalar diffusivity defined as $\kappa = \nu/Pr$. In our simulations, we choose Prandtl number $Pr = 700$, that corresponds to the salinity-induced stratification in water. We note that for stratified flows with $Pr > 1$, the scales are smaller for density than the velocity at a given Re . To resolve the dynamic scales in such a stratified flow, very fine spatial resolution is required (Orr & Constantinescu 2015). In order to estimate the momentum and density boundary layer thickness (l_m and l_d respectively), we adopt the following relations (Schlichting & Klaus 2003):

$$l_m \sim O\left(\frac{d}{\sqrt{Re}}\right) \quad (3.5)$$

and

$$l_d \sim O\left(\frac{d}{\sqrt{RePr}}\right). \quad (3.6)$$

The moderate Reynolds numbers considered in the present work ($Re \leq 356$) allow the application of axisymmetry assumption. A three-dimensional numerical simulation of a particle (sphere) settling in linearly stratified fluid shows that the flow remains axisymmetric at Reynolds number up to 356 without vortex shedding (Doostmohammadi & Ardekani 2014b). It has also been reported that nearly axisymmetric structure is retained even at $Re \sim 800$ (Torres *et al.* 2000). After testing different spatial resolutions, we find that the mesh with approximately 348,000 cells provides satisfactory accuracy. The first cell layer around the particle surface is with the height of $0.0014D$, which grows exponentially at a slow rate normal to the sphere surface. The grid size grows from the surface to a maximum cell length of $0.1D$ at the radial distance $10D$ from the particle centre, and then keeps constant to the outer boundaries. According to (3.5) and (3.6), $l_m \sim 0.053D$ and $l_d \sim 0.002D$ for $Re = 356$ and $Pr = 700$, respectively. Note that the choice of Re here corresponds to the highest Re in our numerical simulations. Though the mesh resolution we adopt satisfies l_d around the vicinity of the sphere surface, we note that the resolution in the far wake region may not resolve the density gradient well. It would be noteworthy to mention that a numerical study by Torres *et al.* (2000) suggested that in a moderate Reynolds number regime, the actual thickness of the density boundary layer can be larger than the predicted value of (3.6). This was also verified by Doostmohammadi & Ardekani (2014b) in their simulations of a settling sphere in a linearly stratified fluid with $Pr = 700$. The authors carried out tests with minimum cell length up to 6 times larger than those predicted from (3.6), and observed little deviation in their results. While high computational cost is a limiting factor for global density boundary layer resolution in the domain, a qualitative examination still shows that our numerical simulations capture the structures evolving in the stratified wake to a good extent.

We solve the governing equations of the stratified flow using finite-volume based

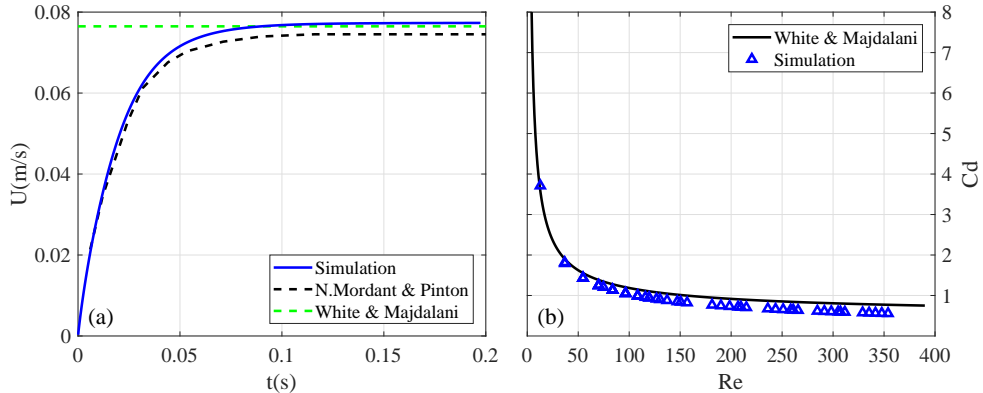


FIGURE 3. (a) Velocity profiles of a particle settling in a quiescent homogeneous fluid at $Re = 41$. (b) Drag coefficients for particles settling in homogeneous fluid.

code (Weller & Fureby 1998). The space discretisations are second-order upwind for the convection terms and central differences for the Laplacian terms, respectively. The time discretisation is second-order implicit Euler. The pressure-velocity coupling is obtained using the PISO (Pressure-Implicit with Splitting of Operators) scheme. For the velocity boundary conditions, we set that on the sphere surface to be moving-wall with no flux normal to the wall. A zero-gradient condition is imposed on all other velocity boundaries. The pressure is fixed at the top boundary. A fixed-flux condition is adopted for the pressure at all other boundaries, such that the velocity boundary condition can specify the flux on those boundaries. The density is fixed at the top and bottom boundaries, with constant values (ρ_u and ρ_l respectively), and a zero-gradient condition for density is imposed on other boundaries.

The numerical methods are tested against experimental results of a particle settling in homogeneous and stratified fluids. The velocity profile of a particle settling in a quiescent homogeneous fluid is compared with the experimental results of Mordant & Pinton (2000), as shown in figure 3(a). The velocity matches the experiment well at the beginning, but is a little bit higher after the particle reaches a steady state. The terminal velocity is dependent on the steady-state drag, which is defined as

$$F_d = -\frac{1}{2}C_d\rho_fU|U|S_p, \quad (3.7)$$

where C_d is the drag coefficient and S_p is the cross-sectional area of the particle. C_d can be calculated by an empirical formula

$$C_d = \frac{24}{Re} + \frac{6}{1 + \sqrt{Re}} + 0.4, \quad (3.8)$$

with error less than 10% for $0 < Re < 2 \times 10^5$ (White & Majdalani 2006). The simulated drag coefficients are presented in figure 3(b), which qualitatively agree with that predicted by (3.8). Further, We test the numerical method with a particle settling in stratified fluid. The transient flow structures are shown in figure 9, comparing to the experiment presented in figure 7. The bouncing behaviour is well captured, as shown in figure 10. The results show that the simulation results agree well with our experiments. Those numerical results will be discussed later in detail.

Parameter	Symbol	Definition	Range of values
Particle density	ρ_p	—	1121.58 ~ 1125.26 kg/m ³
Particle diameter	D	—	10.055 ~ 10.128 mm
Particle velocity	U	—	-0.559 ~ 4.908 cm/s
Jet velocity	u_j	—	—
Upper fluid density	ρ_u	—	1113.92 ~ 1118.63 kg/m ³
Lower fluid density	ρ_l	—	1121.45 ~ 1123.66 kg/m ³
Interface thickness	L	—	2.52 ~ 13.06 cm
Upper Reynolds number	Re_u	$\rho_u U_u D / \mu_u$	115 ~ 356
Lower Reynolds number	Re_l	$\rho_l U_l D / \mu_l$	1 ~ 125
Froude number	Fr	U_u / ND	2 ~ 7
Brunt-Väisälä frequency	N	$\sqrt{(g(\rho_l - \rho_u) / L \rho_{ref})}$	0.62 ~ 1.88
Reference density	ρ_{ref}	$(\rho_u + \rho_l) / 2$	1118.08 ~ 1120.09 kg/m ³
Prandtl number	Pr	ν / κ	~ 700
density ratio	$\Delta \rho_l$	$(\rho_p - \rho_l) / \rho_l$	$(0.03 \sim 2.54) \times 10^{-3}$

TABLE 1. Definition and ranges of parameters covered in the present work.

4. Results and discussion

4.1. Controlling parameters

A particle settling in a stratified fluid is mainly characterised by three non-dimensional parameters, the upper layer Reynolds number $Re_u = \rho_u U_u D / \mu_u$, the lower layer Reynolds number $Re_l = \rho_l U_l D / \mu_l$, and the Froude number $Fr = U_u / ND$, where U is the terminal settling velocity of the particle in a homogeneous upper or lower fluid, μ is the dynamic viscosity of the fluid, D is the particle diameter, and the subscripts u and l represent respectively the upper and lower layer fluids. The Brunt-Väisälä frequency N is calculated as

$$N = \sqrt{\frac{2g}{\rho_u + \rho_l} \frac{\rho_l - \rho_u}{L}}, \quad (4.1)$$

where L is the thickness of the density transition layer, covering 98% of the density variation (figure 2(a)). All relevant parameters are listed in table 1.

4.2. Bouncing process

First, we choose a typical set of parameters, to demonstrate the bouncing process, or levitation (Abaid & McLaughlin 2004), as a particle settles through a density transition layer. The velocity and the acceleration, as well as the visualised flow, of a classical bouncing particle are presented. Here, the non-dimensional parameters are $Re_u = 347$, $Re_l = 20$ and $Fr = 2.5$. At these Reynolds numbers, the flow is nearly axisymmetric thus the particle can stay in the laser-sheet-illuminated plane and be captured during the whole settling process.

The velocity and acceleration of the bouncing particle are presented in figure 4. The deceleration begins before the particle enters the density interface (figure 4(a)), as the existence of the interface limits the vertical excursion of fluid (Ardekani & Stocker 2010). As the particle enters the interface, the velocity decreases more rapidly. The maximum deceleration is reached at approximately the lower bound of the interface. The particle reaches a zero velocity in the lower layer and bounces up, reentering the interface. The bouncing is like a beginning of a damped oscillation, which is more obvious in figure 4(b). Note that the triggered oscillation is not a common feature for a bouncing particle.

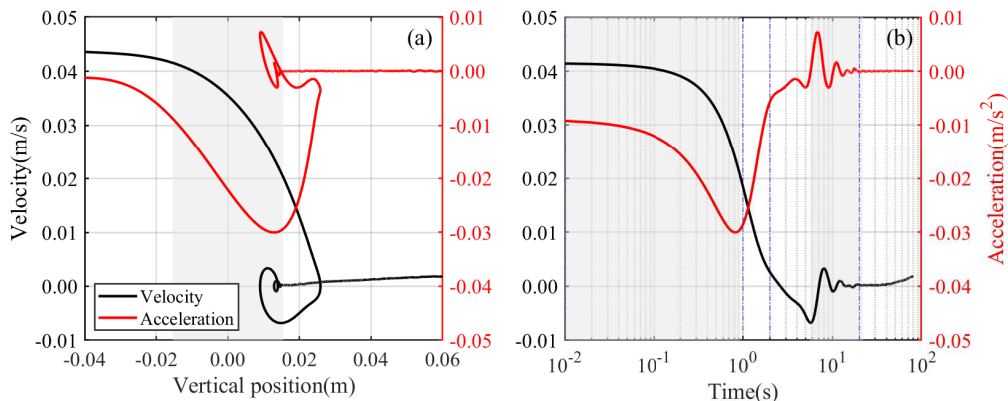


FIGURE 4. Settling velocity and acceleration of the particle with $Re_u = 347$, $Re_l = 20$ and $Fr = 2.5$ as the functions of (a) the vertical position and (b) settling time. The left and right vertical axis correspond respectively to the settling velocity and acceleration. In (a), the vertical position ($z = 0$) refers to the middle plane of transition layer, and the time $t = 0$ refers to the instant when the particle's centre reaches the upper boundary of the transition layer. In (a), the shaded region represents the transition layer, and in (b), the two shaded regions denote when the particle's centre is within the transition layer. Note the right-side shaded region in (b) denotes when the particle re-enters the transition layer after bouncing. In (b), four stages are divided by blues dashed lines.

It occurs only at strong bouncing where the particle could reenter the interface. Finally, the particle accelerates again and slowly approaches its new terminal velocity.

A series of images corresponding to figure 4, showing the development of the wake over the whole settling process, are presented in figure 5. We divide the settling process into four stages, and separate them by vertical dashed lines in figure 4(b). (1) Wake attachment (figure 5(a)-(e)). The particle enters the interface and drags a large amount of upper fluid at its rear. The velocity decreases rapidly and the deceleration reaches its maximum at the end of this stage (figure 4(b)). (2) Wake detachment (figure 5(f)-(j)). At this stage, most of the attached upper fluid (wake) detaches from the particle and returns to its neutral position, although it could hardly return to the upper layer as its density has been increased by the mixing. At the centre axis above the particle, a long thin column of lighter fluid keeps attached. This column does not break but elongates and gets thinner until it is too thin to be captured. The velocity continues to decrease and the acceleration becomes smaller, compared to the first stage (figure 4(b)). By the end of this stage, the particle loses over 90% of its entering velocity U_u . (3) Transient bouncing (figure 5(k)-(q)). The particle reaches a zero velocity ($t = 2.61$ s) and bounces up. Triggered by the rupture of wake, strong internal wave is generated at the interface (figure 6), which causes oscillation of the particle. At this stage, almost all of the lighter fluid has detached from the particle, which indicates that the bouncing of particle is more likely induced by the flow, or specific flow structure, not the buoyancy of wake. More details of the bouncing mechanism will be discussed in section 4.4. (4) Final sedimentation (figure 5(r)-(t)). After the bouncing and oscillation, the particle slowly settles to the bottom of tank. Note the increased time interval between images. The particle settles extremely slowly after passing through the density interface.

These four stages are typical stages that a bouncing particle would experience. Note that the bouncing process begins at the third stage, after the wake detaches from the particle. This is in agreement with the phenomena observed by [Abaid & McLaughlin \(2004\)](#) that the particle changes its moving direction after the ascending of the ‘plume’,

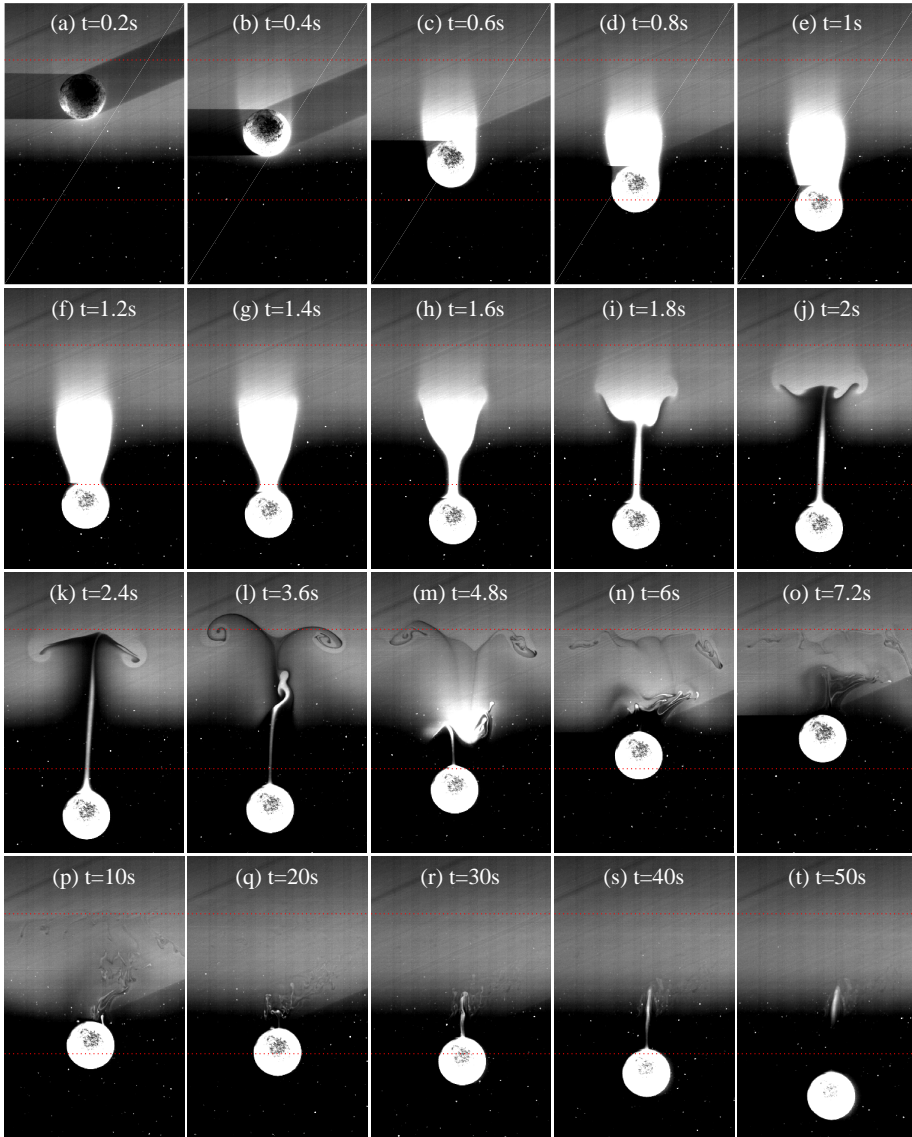


FIGURE 5. A sequence of images showing the bouncing process of a particle settling through a density transition layer, corresponding to figure 4. The two red dashed lines in each image represent the bounds of the interface. The non-dimensional parameters are $Re_u = 347$, $Re_l = 20$ and $Fr = 2.5$.

where the ‘plume’ is actually the detached wake in our experiment. For a monotonously settling particle, the first two stages are same, followed by a final sedimentation without bouncing up.

4.3. Flow structure

To measure the transient flow structure around the particle, PIV and wake visualisation images are captured by two cameras simultaneously, using the experimental setup 2 illustrated in figure 1. In figure 7, we present the results of a bouncing particle with non-dimensional parameters $Re_u = 198$, $Re_l = 20$ and $Fr = 2.3$. Initially, the flow

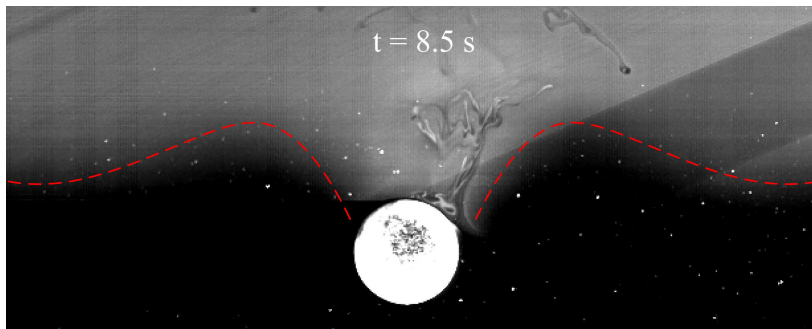


FIGURE 6. Full image of internal wave at $t = 8.5\text{s}$ between figure 5(o) and 5(p).

around the particle is similar to that in a homogeneous fluid. After entering the interface, accompanying the rupture of the wake, a vortex with direction opposite to that in the homogeneous fluid, is formed at the rear of the particle. It quickly grows and detaches from the particle, becomes a vortex ring remaining at the interface (figure 7(d)(e)). As explained in the previous work (Zhang & Magnaudet 2019; Magnaudet & Mercier 2020), this vortex is sourced from the baroclinic torque caused by the misalignment between the density and pressure gradients.

A close view of the flow around the particle is presented in figure 8. At the rear of the particle, an upward jet (according to a negative u_z) is generated along the central axis. The jet structure has been widely reported in linearly stratified fluid (Torres *et al.* 2000; Hanazaki & Okamura 2009; Zhang & Magnaudet 2019), which was believed to be caused by the continual dragging and rupture of the lighter fluid. In our experiment, the jet is transient as the dragging and rupture of lighter fluid are temporal processes. The jet forms as the wake breaks (figure 8(c)), and decays faster thereafter. As the particle bounces (figure 8(g)), the jet is a dominating structure at the vicinity of the particle. It is reasonable to deduce that the bouncing of particle is caused by the pull of the jet (as discussed in section 4.4.3). However, we find that the occurrence of jet is quite common for a particle settling at moderate Reynolds numbers, even without bouncing motion. The jet is actually accompanied with the aforementioned wake detachment, which is observed throughout the parameter range. As we will attempt to address that the jet is a necessary but not sufficient condition for bouncing.

4.4. Force analysis

As we know, the nonmonotonic motion of a particle settling in a stratified fluid is caused by a so-called ‘stratification drag’ (noted as F_s). Previous studies revealed that F_s is mainly contributed by two mechanisms: the buoyancy of dragged upper fluid and the force caused by a specific flow structure (Srdić-Mitrović & Fernando 1999; Zhang & Magnaudet 2019; Higginson & Linden 2003; Yick *et al.* 2009). In this section, we analyse the force acting on a bouncing particle, to further understand the mechanism of the bouncing behaviour. For the convenience of force decomposition, we present the numerical results of a settling particle with the setups matching that of the experiments in section 4.3. The simulated non-dimensional parameters are $Re_u = 198$, $Re_l = 26$ and $Fr = 2.3$. The simulated density field is presented in figure 9, which exhibits the same wake structure with that in the experiment. Due to the difference of the lower Reynolds number, the bouncing behaviour is more obvious in experiment, as shown in figure 10. We detail in section 4.5.1 that the occurrence of bouncing depends mainly on Re_l . Overall, the simulation results are in agreement with the experiments.

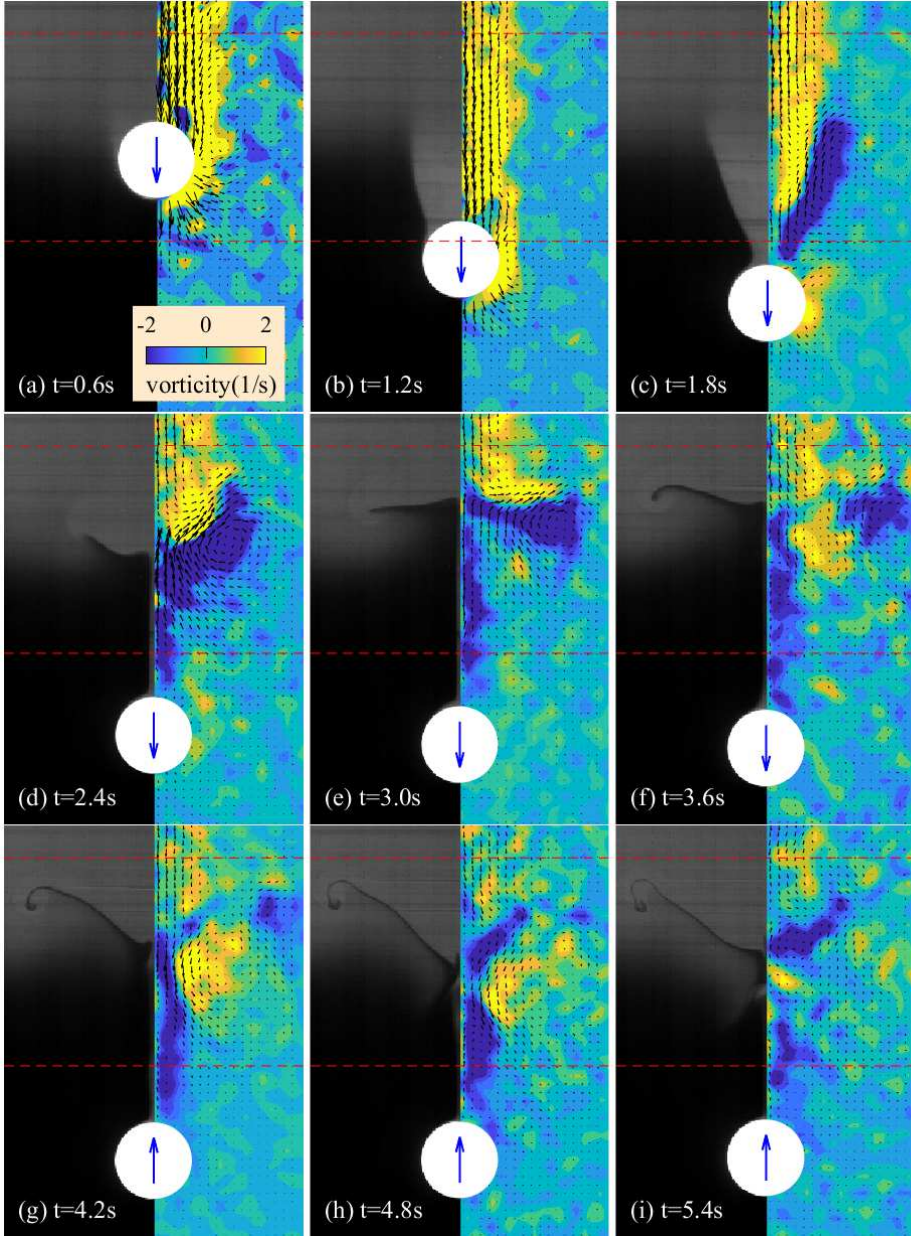


FIGURE 7. Illuminated wake (left) and PIV fields (right) of a particle settling through a density transition layer at $Re_u = 198$, $Re_l = 20$ and $Fr = 2.3$. The horizontal red dashed lines mark the bounds of the interface. The arrows at the particle centre point to the moving direction of the particle.

We present the force analysis by three steps. (1) Introduce how we decompose the force. (2) Describe how we calculate the force components. (3) Present the forces acting on a bouncing particle and analyse the bouncing mechanism.

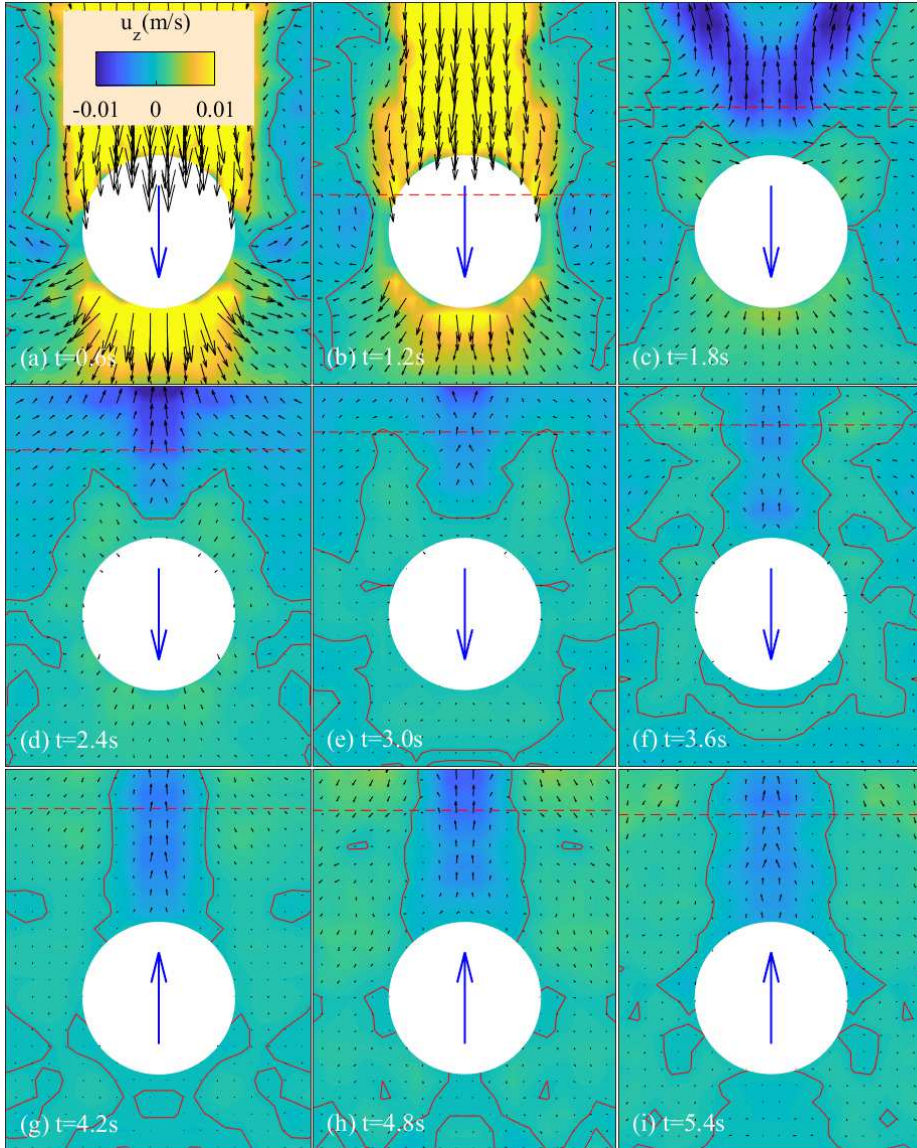


FIGURE 8. A close view corresponding to the vicinity around the particle of figure 7. The red solid lines are isolines of $u_z = 0$. An upward jet is generated at the centre axis behind the particle.

4.4.1. Force decomposition

To understand the underlying physics of particle bouncing behaviour, we attempt to decompose its hydrodynamic force into different components. We start from the motion equation of a particle settling from the rest in a quiescent homogeneous fluid, which can be written as

$$m_p \frac{dU}{dt} = G + F_b + F_d + F_a + F_h. \quad (4.2)$$

The left-hand side is the total inertia force acting upon the particle, where m_p is the particle mass. It arises due to the imbalance of forces. At the right-hand side, G and F_b are respectively the gravity and buoyancy forces of the particle, F_d is the ‘steady-state’

drag force at the considered time instant, F_a is the inertia force of added mass, and F_h is the history (Basset) force. Here, F_d can be evaluated according to (3.7) and (3.8). In the limit of potential flow, F_a can be calculated as

$$F_a = -\frac{1}{2}\rho_f V_p \frac{dU}{dt}. \quad (4.3)$$

At the Stokes regime, F_h has an analytic solution

$$F_h = -\frac{3}{2}D^2\sqrt{\pi\rho_f\mu} \int_{-\infty}^t \frac{\dot{U}(\tau)}{\sqrt{t-\tau}} d\tau. \quad (4.4)$$

For the particle settling in a stratified fluid, we follow the same way of drag force decomposition as in (4.2), while introducing an extra term F_s , accounting for the stratification effects. The motion equation becomes

$$m_p \frac{dU}{dt} = G + F_b + F_d + F_a + F_h + F_s. \quad (4.5)$$

It is reasonable to further decompose F_s into two components as

$$F_s = F_{sb} + F_{sj}, \quad (4.6)$$

where F_{sb} is the enhanced buoyancy caused by dragging the upper fluid to the lower layer, therefore modifying the density distributions, and F_{sj} is the force caused by the induced flow structure due to the stratification, represented typically by the upward jet flow at the rear of the particle. As we have discussed in figure 8, the observed jet is conjectured to be the dominant flow structure as the particle bounces. The equation of motion for a particle settling in a stratified fluid can therefore be written as

$$m_p \frac{dU}{dt} = G + F_b + F_d + F_a + F_h + F_{sb} + F_{sj}. \quad (4.7)$$

4.4.2. Force calculation

It is possible to evaluate numerically the different force components. The most convenient way is to reorganise (4.7) as

$$m_p \frac{dU}{dt} = G + \underbrace{(F_b + F_{sb})}_{F_{static}} + \underbrace{(F_d + F_a + F_h + F_{sj})}_{F_{dynamic}}, \quad (4.8)$$

where F_{static} is the hydrostatic force caused by density stratification and its nonuniform distributions, and $F_{dynamic}$ is the force caused by the non-zero velocity field at uniform density distribution. Excluding the steady-state drag F_d , the sum of $(F_a + F_h + F_{sj})$ represents the force caused by unsteady flow, i.e., the flow caused by the stratification effect. For a given density field, the hydrostatic pressure p_s can be obtained by solving

$$\nabla p_s = \rho g. \quad (4.9)$$

F_{static} is the integration of p_s over the particle surface:

$$F_{static} = - \int_S p_s \mathbf{n} dS, \quad (4.10)$$

where \mathbf{n} is the unit normal at the surface. Since F_b can be calculated by considering an undisturbed density profile, we have

$$F_{sb} = F_{static} - F_b. \quad (4.11)$$

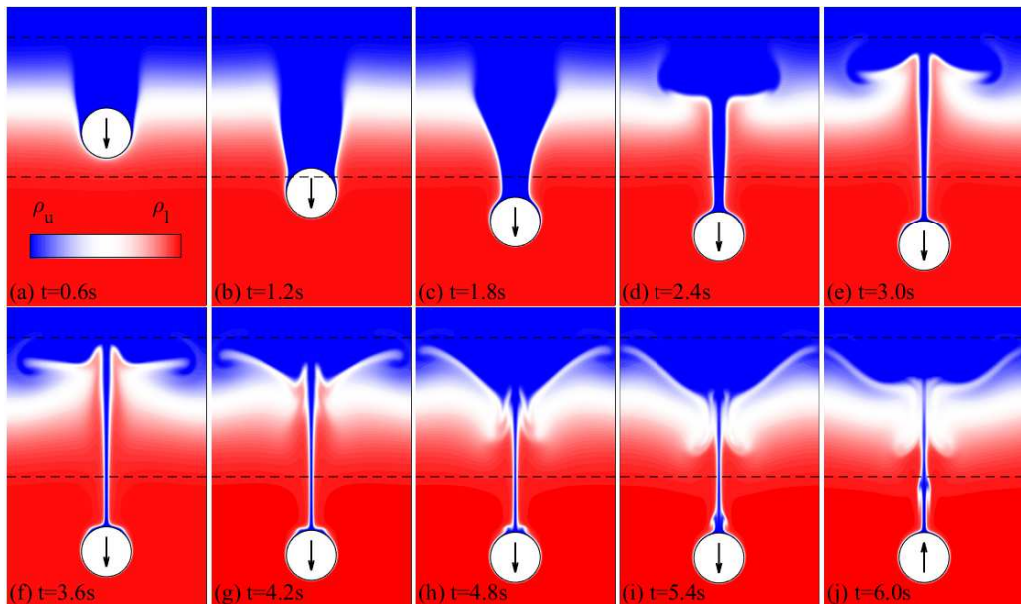


FIGURE 9. Development of simulated density field of a particle settling through a density transition layer at $Re_u = 198$, $Re_l = 26$ and $Fr = 2.3$, presented as a comparison with the experiment shown in figure 7.

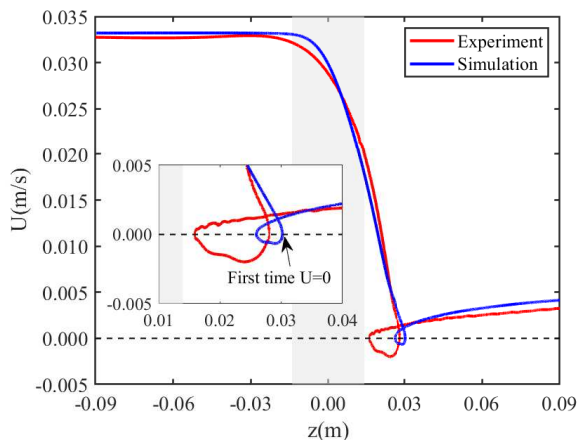


FIGURE 10. Comparison between the simulated and experimental velocity profiles at $Re_u = 198$ and $Fr = 2.3$. Note that the lower Reynolds number for simulation is $Re_l = 26$, while that for the experiment is $Re_l = 20$.

The total hydro-force F_{hydro} acting on the particle, i.e., $F_{static} + F_{dynamic}$, can be calculated by solving the equations (3.1), (3.3) and (3.4). Then, we have

$$F_{dynamic} = F_{hydro} - F_{static}. \quad (4.12)$$

If we evaluate the steady-state drag F_d using (3.7) and (3.8), we can write the drag component contributed by unsteady flow as

$$F_{sj} + F_a + F_h = F_{dynamic} - F_d. \quad (4.13)$$

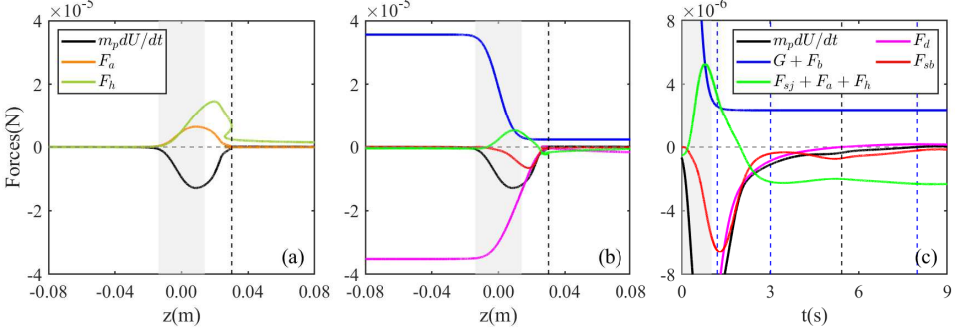


FIGURE 11. Decomposed forces of a bouncing particle at $Re_u = 198$, $Re_l = 26$ and $Fr = 2.3$, corresponding to figure 10. The shadow area represents the interface region. The black dashed lines show the inception of the bouncing behaviour. In figure (c), the four stages are separated by blue dashed lines, which are: wake attachment, from $t=0$ to the first blue dashed line; wake detachment, from the first to the second blue dashed line; transient bouncing, from the second to the third blue dashed line; final sedimentation, from the third blue dashed line to the end.

4.4.3. Forces of a bouncing particle

For a particle settling through a density interface, if $U_{min} \leq 0$ (keeping in mind that the positive direction of z -axis points downwards), it bounces up. At the instant when the first time the particle reaches $U = 0$ (see the arrow in figure 10), the particle satisfies

$$\frac{dU}{dt} < 0. \quad (4.14)$$

Thus at $U = 0$ we have

$$m_p \frac{dU}{dt} = \underbrace{G + F_b}_+ + \underbrace{F_d}_0 + \underbrace{F_a}_+ + \underbrace{F_h}_+ + \underbrace{F_{sb}}_- + \underbrace{F_{sj}}_- < 0. \quad (4.15)$$

In figure 11(a), we plot F_a and F_h predicted by (4.3) and (4.4). We note that the solutions given by (4.3) and (4.4) can actually not be accurately applied to our Reynolds number ($Re_u \approx 200$). However, at least we know that F_a and F_h are opposite to the acceleration of the particle, i.e, positive at this time instant. Apparently, the necessary condition for (4.15) to hold is

$$|F_{sb}| + |F_{sj}| > |G + F_b|. \quad (4.16)$$

Whether the jet is necessary for the occurrence of bouncing depends on the magnitude of F_{sb} . When $|F_{sb}| \leq |G + F_b|$, the contribution of jet is necessary for the bouncing behaviour. Observed from our experiments, as discussed in section 4.2, the particle reverses its motion direction after the wake detaches, so that F_{sb} is relatively small, therefore F_{sj} is determinant for the bouncing behaviour.

The decomposed force components as the functions of vertical position is plotted in figure 11(b), where $(G + F_b)$ is the reduced gravity. Since F_a and F_h cannot be accurately calculated, we plot $(F_{sj} + F_a + F_h)$, which is the force due to the unsteady flow, and also gives the upper limit of F_{sj} . Note that $(F_a + F_h)$ is always positive during the settling process. Apparently, before entering the transition layer, the balance between the reduced gravity $(G + F_b)$ and the drag force F_d makes the particle reach a constant settling velocity. As the particle enters the transition layer, the force components $m_p dU/dt$, F_{sb} and $F_{sj} + F_a + F_h$ arise from their nearly zero values. We also present the time histories of different force components in figure 11(c), with the aforementioned four stages (section

Experiment series	Test number	ρ_u (kg/m ³)	ρ_l (kg/m ³)	L (cm)	Minimal velocity (cm/s)				
					P1	P2	P3	P4	P5
series 1	1	1116.52	1123.66	3.14	-0.492	-0.228	0.304	0.578	0.889
	2	1116.52	1123.32	3.01	-0.140	0.237	0.560	0.780	1.048
	3	1116.52	1123.01	2.92	0.250	0.468	0.735	0.952	1.218
	4	1116.55	1122.71	2.86	0.415	0.610	0.858	1.059	1.302
	5	1116.52	1122.39	2.52	0.683	0.835	1.067	1.249	1.467
series 2	6	1115.05	1121.87	2.71	-0.397	0.015	0.454	0.712	0.994
	7	1115.90	1121.85	3.22	-0.324	0.114	0.497	0.739	1.025
	8	1116.86	1121.85	3.23	-0.414	-0.100	0.376	0.648	0.939
	9	1117.97	1121.95	3.02	-0.337	0.064	0.475	0.742	1.022
	10	1118.63	1121.45	3.67	-0.162	0.137	0.516	0.781	0.985
series 3	11	1113.93	1122.24	3.15	-0.559	-0.214	0.336	0.616	0.879
	12	1113.92	1122.24	6.72	-0.248	-0.087	0.376	0.651	0.922
	13	1113.92	1122.24	9.83	-0.117	0.014	0.371	0.639	0.928
	14	1113.92	1122.24	11.53	-0.035	0.103	0.435	0.705	0.954
	15	1113.92	1122.24	13.06	0.013	0.118	0.461	0.724	0.993

TABLE 2. Experimental parameters and the minimal velocities.

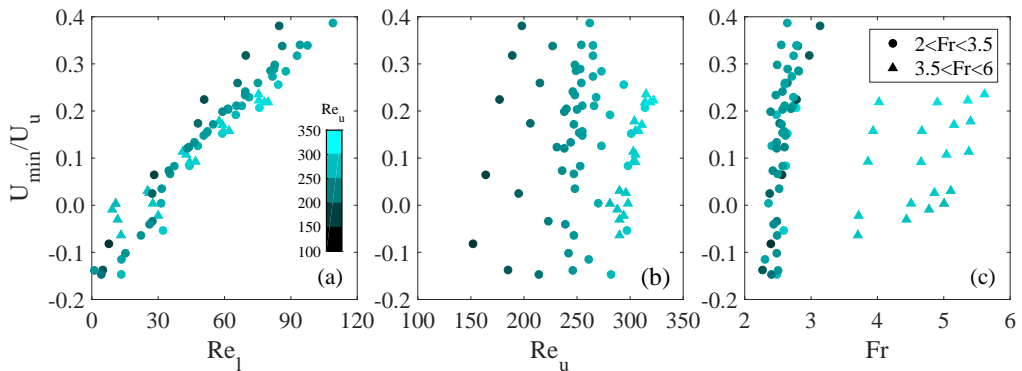
4.2) separated by three blue dashed lines. The wake buoyancy force F_{sb} correlates to the volume of attached upper light fluid. It reaches a maximum at the end of the first stage, after the dragging of the wake (see figure 9(b) for $t = 1.2s$), and before the wake detaches from the particle. The sharp rise of $(F_{sj} + F_a + F_h)$ (the green line) is dominated by $(F_a + F_h)$ at the first two stages due to the sudden deceleration of the particle. As approaching the third stage, F_{sb} becomes small since only a thin layer of light fluid left in the attached wake (see figure 9(e) for $t = 3.0s$). In the mean time, $(F_{sj} + F_a + F_h)$ appears to be the dominant drag force (to balance the reduced gravity $(G + F_b)$), arresting further settling of the particle. At the instant of bouncing occurrence, the settling velocity U approaches zero (marked by the black dashed line in figure 11 and see also figure 9 between $t = 5.4s$ and $t = 6.0s$). At this time, $|F_{sb}| \ll |G + F_b|$, and $(F_{sj} + F_a + F_h)$ plays a dominant role in balancing the reduced gravity. Excluding $(F_a + F_h)$, the contribution from F_{sj} takes the primary part of the drag force. Therefore we conjecture that the jet flow is a necessary condition for bouncing the particle up. In conclude, we prefer to the interpretation that F_{sb} is the primary factor for decelerating the particle as it enters the transition layer, while F_{sj} induced by the jet flow further decelerates the particle till reverses its motion as it leaves the transition layer.

4.5. Influence of different parameters

We carry out a parametric study by varying the controlling parameters. Three series of experiments are conducted. Each series includes five tests, as listed in table 2. We vary the lower fluid density ρ_l , upper fluid density ρ_u , and the interface (transition layer) thickness L to get different lower layer Reynolds number Re_l , upper layer Reynolds number Re_u , and Froude number Fr . For each test, five particles with slightly different properties (as listed in table 3) are released. The minimal velocity U_{min} that a particle reaches for each release has also been included in table 2. Note that the negative U_{min} implies

Particle number	Diameter (mm)	Density (kg/m ³)
P1	10.075	1121.58 – 1123.74
P2	10.128	1121.86 – 1124.00
P3	10.083	1122.28 – 1124.60
P4	10.075	1122.73 – 1124.79
P5	10.055	1123.18 – 1125.26

TABLE 3. Particle properties.

FIGURE 12. The minimal velocity of all the particles in experiments versus upper, lower Reynolds numbers and Froude number. $U_{min}/U_u < 0$ represents a bouncing behaviour.

the occurrence of bouncing. Since the particle density varies with ambient temperature, before each test, the particle density is precisely measured to an accuracy of 0.01 kg/m³.

The non-dimensional minimal velocities versus Re_l , Re_u and Fr for all the collected experimental data are shown in figure 12. Clearly, the minimal velocity (U_{min}/U_u) correlates more strongly to the lower Reynolds number ($Re_l = 1 \sim 109$) than the upper Reynolds number ($Re_u = 152 \sim 322$) and the Froude number ($Fr=2.3 \sim 5.6$). The bounce is seen to occur as Re_l is smaller than about 30.

4.5.1. Lower Reynolds number Re_l

To further investigate the relationship between the minimal velocity and the lower Reynolds number, the experimental data from series 1, where the upper Reynolds number and Froude number are $Re_u = 252 \pm 16$ and $Fr = 2.6 \pm 0.2$ respectively, are plotted over the lower Reynolds number Re_l in figure 13(a). The numerical results at $Re_u = 258$ and $Re_u = 349$ with the fixed Froude number $Fr = 2.6$ are also plotted for comparison. From the trend, the experimental and numerical results are consistent, both indicating that U_{min}/U_u increases linearly with Re_l . We note that for $Re_u \sim 252$, the values of U_{min}/U_u in the experiments are uniformly higher than that of the simulations, which is possibly caused by the incomplete development of U_l in the experiments. After passing through the interface, a long distance is required for the particle to reach a steady state velocity. Such that the velocity measured at the instant when the particle leaves the viewing window in our experiments might be smaller than the fully developed U_l in the simulations, resulting a smaller Re_l . We can fit the data shown in figure 13(a) by the

lines expresses as

$$\frac{U_{min}}{U_u} = c_1 Re_l + c_2. \quad (4.17)$$

The linear regression gives $c_1 = 0.0049$ and $c_2 = -0.1181$ for the experiments ($Re_u = 252 \pm 16$), and $c_1 = 0.0046$ and $c_2 = -0.1720$ for the numerical results ($Re_u = 258$). Critical lower Reynolds numbers $Re_l^* = 23.9$ and 37.5 are identified respectively for these two lines, i.e., the position intersected with the horizontal axis, or when $U_{min} = 0$. It is easy to understand that the undetermined parameters c_1 and c_2 are dependent on Re_u and Fr . Evidenced from 13(a), with a higher upper Reynolds number $Re_u = 349$, the fitting line gives a smaller slope compared with both the experiments and simulations with the smaller Reynolds numbers. However, it is interesting to find that the critical lower Reynolds numbers Re_l^* obtained from the numerical simulations with different Re_u are very close.

In our experiments, since the terminal Reynolds numbers are not known *a priori*, we practically adjust the fluid density to get varied Reynolds numbers. Previous works show that the bouncing behaviour is related to the fluid density and density ratio (Camassa & Vaidya 2022; Doostmohammadi & Ardekani 2014a). Thus the relationship between the minimal velocity and the density ratio should also be investigated. Here, we define the density ratio as $\Delta\rho_l = (\rho_p - \rho_l)/\rho_l$. Since Re_l is correlated to the density difference, the relationship between U_{min} and $\Delta\rho_l$ can be derived from (4.17). For a particle settling to a steady-state velocity in a homogeneous fluid, the drag force balances the reduced gravity, satisfying the following expression:

$$F_d = G - F_b. \quad (4.18)$$

Using the definition of F_d in equation (3.7) and substituting $U_l = \nu_l Re_l/D$ into (4.18), we get the following expression between density ratio and Reynolds number:

$$\Delta\rho_l = \frac{3C_{dl}\nu_l^2 Re_l^2}{4gD^3}, \quad (4.19)$$

where C_{dl} is the steady-state drag coefficient in the lower layer. Equations (4.17) and (4.19) yield

$$\frac{U_{min}}{U_u} = c_1 \sqrt{\frac{4gD^3}{3\nu_l^2 C_{dl}}} \Delta\rho_l^{\frac{1}{2}} + c_2. \quad (4.20)$$

We find that the power law fitting in the form

$$\frac{U_{min}}{U_u} = c_3 \Delta\rho_l^{\frac{1}{2}} + c_4, \quad (4.21)$$

is appropriate to describe the dependence of U_{min}/U_u on $\Delta\rho_l$, as shown in figure 13(b) (recompiling the data from figure 13(a)).

The trajectories and velocity profiles of particle P1 from the experiment series 1 are plotted in figure 14. It is clearly shown in figure 14(a) that the sedimentation time is dramatically prolonged by the bouncing behaviour. Although the particle enters the interface with the same velocity, the slight variation of Re_l significantly alters the behaviour. For a relatively large lower layer Reynolds number, e.g. $Re_l = 59$, though a minimum velocity is observed in figure 14(b), the particle keeps descending unidirectionally after it passes through the transition layer. We emphasise that all particles have larger density than the fluid in the tank at all attitudes. As Re_l decreases, crossing a critical value, i.e. Re_l^* , as we have discussed above, the particle reverses its direction of motion and ascends for a transient time scale (see figure 14(a) for $Re_l = 26$

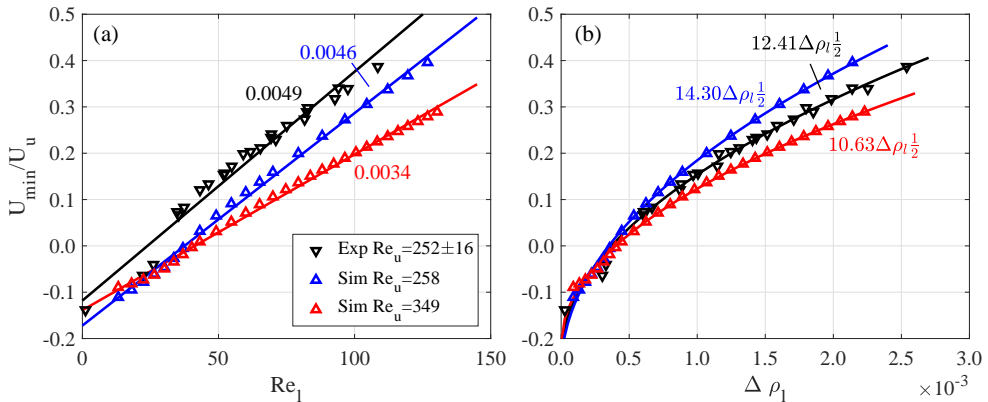


FIGURE 13. The variations of non-dimensional minimum velocity over (a) Re_l and (b) $\Delta\rho_l$. The Froude number are $Fr = 2.6 \pm 0.2$ for experiment and $Fr = 2.6$ for simulation.

and $Re_l = 1$). This bouncing phenomenon is represented by a much deeper and negative minimum velocity shown in the depth vs velocity plot of figure 14(b). Here, $Re_l = 1$ refers to a very extreme case, when the particle density ($\rho_s = 1123.69 \text{ kg/m}^3$) is near the density of the bottom layer ($\rho_l = 1123.66 \text{ kg/m}^3$). In this case, the particle experiences an extraordinarily long transient time scale to reach the terminal velocity of the bottom layer. An explanation for this long transient, given by the previous study (Abaid & McLaughlin 2004), is that once the plume of upper layer fluid has shed, there still exists around the particle a small boundary layer of upper fluid which diffuses exceptionally slowly due to the very long diffusion time of salt in water and the absence of a strong turbulence diffusion in this low-speed flow state. This is evidenced by our experimental results in figure 5(p~t), which show clearly that a few light fluid remains at the particle surface after the bouncing.

It is worthy mentioning some previous studies, where the bouncing behaviour was not observed. Srdić-Mitrović & Fernando (1999) presented the time trajectories of particles obtained by a series of experiments (see their figure 9). They reported the noticeable decrease of velocity within the transition layer, however without finding reverse motion of the particle. It can be possibly explained from two aspects. First, in their experiments, the upper fluid was a mixture of ethyl alcohol and water, which diffuses faster than salty water. Thus the lighter upper fluid dragged by the particle could adjust to the surrounding fluid immediately and weaken the deceleration of the particle. Second, and more importantly, their examined upper Reynolds numbers fall in the range $0.7 \leq Re_u \leq 23$, much lower than the current studies. As we will discuss later, the upper Reynolds number is also one of the influencing factors for the occurrence of bouncing behaviour. Actually, the second explanation can also be related to a deeper physical mechanism, the rear buoyant jet, which disappears when Re_u is low. As evidenced from the work by Yick *et al.* (2009), there was no sign of such a jet as $Re_u \sim 1$.

4.5.2. Froude number Fr

We now address the effects of Froude number. Referring to the experiment series 3 presented in table 1, we fix both the upper and lower layer fluid densities, varying only the transition layer thickness. This is achieved by releasing the particles in the same tank of fluid with a time interval of 24 hours. The diffusion of salt along such a long time scale gives the variations of transition layer thickness in the range $L = 3.15 \text{ cm} - 13.06 \text{ cm}$, resulting in various Froude numbers.

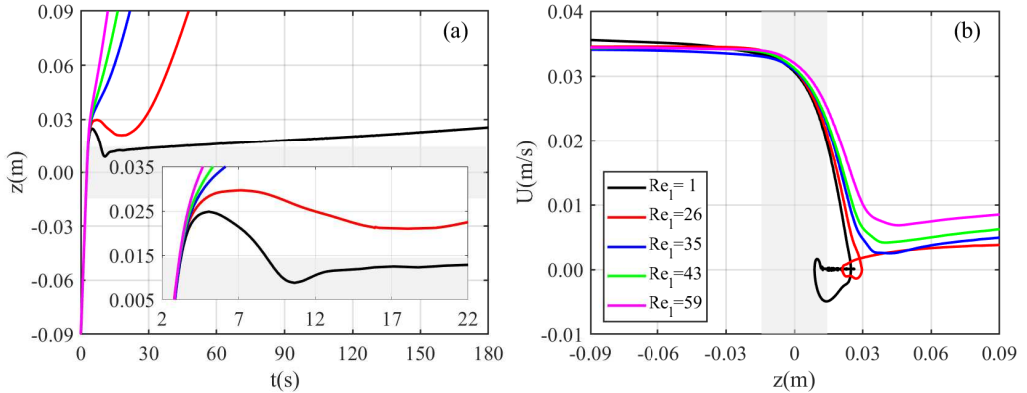


FIGURE 14. (a) Time trajectories of particles at five different lower Reynolds numbers. The nonmonotonic trend indicates a bouncing behaviour. (b) The velocity profiles of particles at five different lower Reynolds numbers. The grey region refers to the density transition layer. Fr and Re_u vary slightly within $Fr = 2.4 \sim 2.5$ and $Re_u = 236 \sim 246$.

We plot the non-dimensional minimum velocities for different particles over the Froude number in figure 15(a). Note that the particle density increases from P1 to P5, therefore both the upper and lower Reynolds numbers increase from P1 to P5. The general trend is a nearly monotonous increase in the non-dimensional minimal velocity along with the increasing Froude number, i.e., as the transition layer becomes thicker. Comparing between the tests of different particles, we can see an overall increase in the minimum velocity when the particle density increases, or equivalently when the Reynolds number increases. Another trend is the less role of Froude number playing in the increase of minimum velocity when the particle density is large (see P5 in figure 15(a)). In contrast, for the lighter particles, such as P1 and P2, the influence of Froude number is remarkable. For example, the behaviour of particle P2 is altered from bouncing to unidirectional settling as the Froude number increases from $Fr = 2.6$ to 5.1. Note that in the tests of P2, the lower Reynolds number ($Re_l = 28$) is very close to the critical Reynolds number Re_l^* . In figure 15, for P3, P4 and P5, no bouncing phenomenon is recorded.

Specifically, we present the velocity profiles of particle P2 at different Froude numbers in figure 15(b). In these tests, the Froude number significantly alters the evolving profile of particle settling velocity. We emphasise that the bouncing motion occurs after the particle leaves the transition layer (see $Fr=2.6$ and 3.7 in figure 15(b)), while the minimum velocity is reached within the transition layer for those tests without bouncing (see $Fr=4.5$, 4.9 and 5.1 in figure 15(b)). There is an interesting phenomenon we want to report. In figure 15(b) we observe that the particle restores to a higher settling velocity for the lower Froude number tests than that with high Froude numbers. It might be caused by the more pronounced diffusion induced by the jet flow. Clearly, the jet flow can enhance the turbulence diffusion and diffuse the remaining upper layer fluid attached on the particle to its ambient lower layer fluid.

4.5.3. Upper Reynolds number Re_u

We next investigate the effects of upper Reynolds number Re_u by numerical simulations. In figure 16(a), the non-dimensional minimal velocity versus Re_u at five different values of Re_l are presented, at a fixed Froude number $Fr = 2.6$. The trend is clear: the minimal velocity increases with the increased lower Reynolds number Re_l , while at a fixed Re_l the minimal velocity decreases with the increase of Re_u except for $Re_l = 13$,

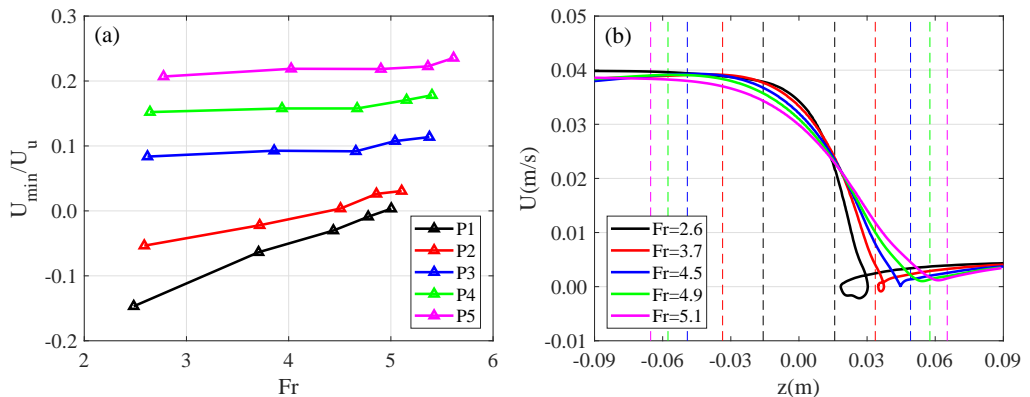


FIGURE 15. (a) The non-dimensional minimum velocity versus Froude number for five particles. The lower and upper Reynolds numbers are: P1, $Re_l = 12$, $Re_u = 286$; P2, $Re_l = 28$, $Re_u = 295$; P3, $Re_l = 44$, $Re_u = 303$; P4, $Re_l = 59$, $Re_u = 306$; P5, $Re_l = 77$, $Re_u = 317$. (b) The velocity profiles of particle P2 versus the vertical position at five Froude numbers. The Vertical dashed lines indicate the bounds of the density transition layers.

where all minimal velocities are negative, indicating the occurrence of bouncing for all cases. We examine a special case, $Re_l = 37$, when the minimum velocity becomes negative as the upper Reynolds number rises to $Re_u = 292$. In figure 16(b), we plot the variations of settling velocity with depth for this special case. Despite the distinct differences in entering velocities of the particle among different tests, their minimal velocities are considerably resembling. Also, they reach minimal velocities at nearly the same depth. Note that the thickness of transition layer varies little among different tests. From figure 12 we understand that $Re_l = 37$ is near the critical Reynolds number for the occurrence of bouncing, therefore this special case is very sensitive to the parameters, such as the upper Reynolds number Re_u . As demonstrated in figure 16(b), the particle moves unidirectionally for $Re_u = 127, 190$ and 244 , while reverses its motion direction for $Re_u = 292$ and 337 .

We thus stress that the upper Reynolds number Re_u plays a non-negligible role only when the bottom layer Reynolds number Re_l is close to its critical value for bouncing. However, we note that the currently studied upper Reynolds numbers, in both experiments and numerical simulations, are kept at a certain order of $Re_u \sim O(100)$, while a much lower Re_u , e.g. in the order $\sim O(1)$ will give no sign of bouncing, as we have discussed in section 4.5.1.

4.5.4. Identification of bouncing regime in (Re_u, Fr) space

Since the bouncing behaviour is primarily determined by the lower Reynolds number Re_l , while the other two parameters, Re_u and Fr can also play their roles, as we have discussed in section 4.5.2 and 4.5.3, it is possible to give a better visualisation by examining their combined effects. For example, in figure 17, we draw two maps in the parametric space of Re_u and Fr for two selected lower Reynolds numbers $Re_l = 13$ and $Re_l = 37$, with the contours representing their minimal velocities. Clearly, the bouncing phenomenon occurs at the higher Re_u and lower Fr , i.e. the upper-left regimes of the maps. The direct comparison between figure 17(a) and (b) indicates that the bouncing regime shrinks for the higher value of Re_l , demonstrating again that Re_l is the dominant parameter. When Re_l is low, the particles are more prone to bounce after passing through the transition layer.

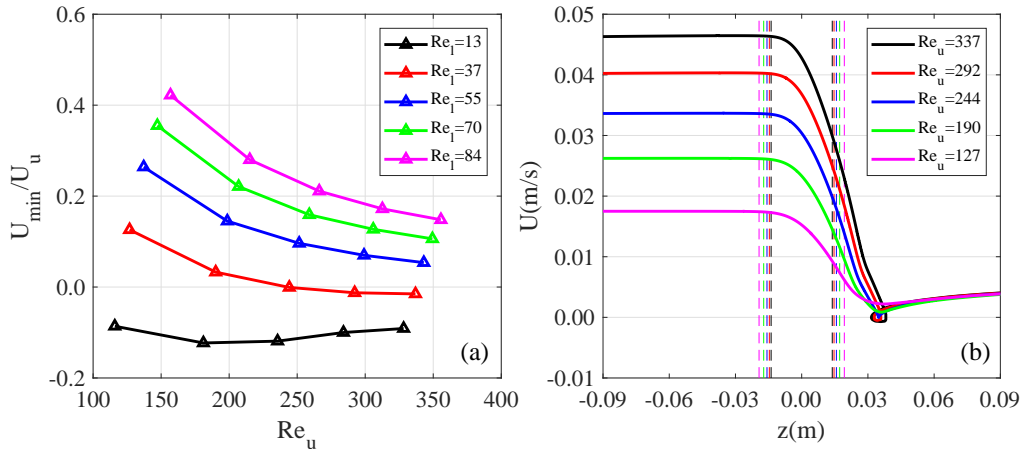


FIGURE 16. (a) The non-dimensional minimal velocity versus the upper Reynolds number at five lower Reynolds numbers, with $Fr = 2.6$. (b) The velocity versus vertical position corresponding to $Re_l = 37$ in (a).

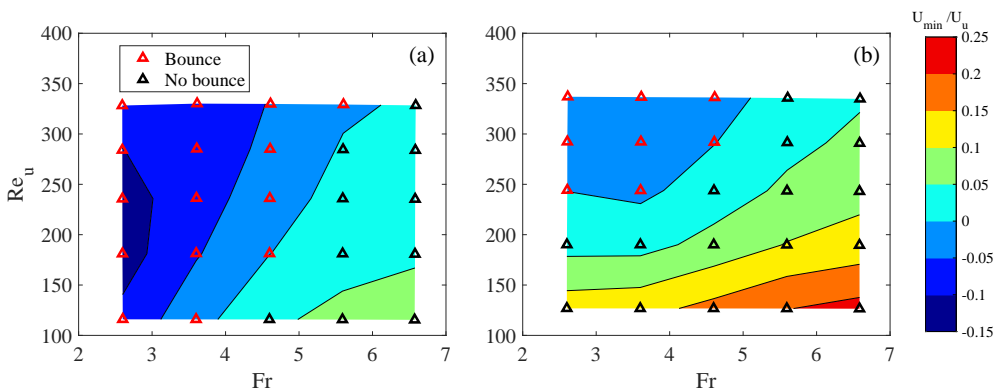


FIGURE 17. Maps of non-dimensional minimal velocities of the settling particle at (a) $Re_l = 13$, and (b) $Re_l = 37$.

	$Fr = 2.6$	$Fr = 3.6$	$Fr = 4.6$	$Fr = 5.6$	$Fr = 6.6$
$Re_u = 349$	41.0	46.2	44.5	25.5	—
$Re_u = 305$	39.6	43.7	39.4	14.4	—
$Re_u = 258$	37.5	40.0	31.9	—	—
$Re_u = 207$	34.6	34.2	21.8	—	—
$Re_u = 147$	28.9	24.3	—	—	—

TABLE 4. Critical lower Reynolds number Re_l^* in the (Re_u, Fr) space.

Simulating in the same (Re_u, Fr) parametric space for different values of Re_l , with a lower limit of $Re_l = 13$, we summarise the critical lower Reynolds numbers Re_l^* in table 4. We note that those with $Re_l < 13$ are not presented in this table. We see that Re_l^* varies from 14.4 to 46.2 depending on different combinations of Re_u and Fr . We should point out that the variations of Re_l^* with Fr at a fixed Re_u are not always monotonous, particularly when Re_u is high.

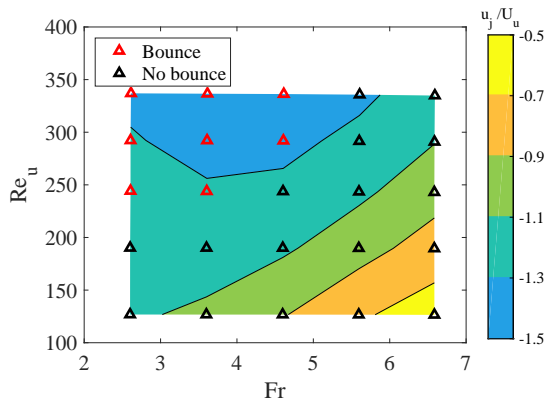


FIGURE 18. Jet velocities with maximum magnitudes in Re_u - Fr space at $Re_l = 37$. The negative value refers to an upward jet.

4.6. Discussion on the strength of buoyant jet

It is worth examining the jet flow by quantifying its strength. Corresponding to figure 17(b), we present the maximum jet velocity for each combination of Re_u and Fr in figure 18. Here, the lower Reynolds number is fixed at $Re_l = 37$. The maximum magnitude of jet velocity is identified at each test, which is scaled by the upper layer terminal velocity U_u . This non-dimensional jet velocity u_j/U_u increases in its magnitude with the increased Re_u while with the decreased Fr , indicating that the jet strength becomes stronger as the inertial effect becomes dominant, as well as the stratification becomes stronger. Not surprisingly, we find that the strong jet region exhibited in figure 18, the upper-left corner, matches well with the bouncing regime shown in figure 17(b). In other words, the upward jet flows correlate to the occurrence of bouncing behaviour.

5. Conclusions

In the present study, we carry out comprehensive experimental tests and numerical simulations on a spherical particle settling through a density stratified fluid, focusing on revealing the physical mechanisms for bouncing behaviour, or reverse motion, as the particle passes through the transition layer. Our study covers a wide range of parameters, with the lower layer Reynolds number $1 \leq Re_l \leq 125$, the upper layer Reynolds number $115 \leq Re_u \leq 356$, the Froude number $2 \leq Fr \leq 7$, and the Prandtl number $Pr \approx 700$ for a salinity-stratified fluid.

First, we decompose the forces acted on the particle into different components, and correlate them to the flow structure. We find that the particle experiences four sequential stages as it settles, in the order of wake attachment, wake detachment, transient bouncing and final sedimentation. Two mechanisms are identified, which contribute to the drag enhancement. First, the buoyancy of attached upper, lighter, fluid and the second, the force caused by a specific flow structure, the buoyancy jet flow. At the first two stages, the force component F_{sb} due to the attached upper fluid in the wake contributes mostly to the drag enhancement. While, at the third stage, most of the upper fluid has detached from the particle, thus F_{sb} becomes less significant. Instead, the force component F_{sj} induced by the jet flow, caused by the rapture of the wake, appears to be dominant. This jet flow is evidenced from our experimental measurements. We conjecture that the jet flow is a necessary condition for the occurrence of bouncing motion.

Then, we investigate respectively the influence of Re_l , Re_u and Fr . We monitor the minimal settling velocity of the particle, of which a negative value indicates a bouncing motion of the particle, hence the bouncing regimes can be clearly identified in the parametric spaces. We find that the lower Reynolds number Re_l is the determinant factor. In our experiments, the bouncing motion is found to occur below a critical lower Reynolds number around $Re_l^* = 30$. In the numerical simulations, the highest value for this critical number is $Re_l^* = 46.2$, limited in the currently studied parametric ranges. Moreover, by examining the jet flow by quantifying its strength, we find a consistency between the maximum magnitude of jet velocity in the flow fields and the minimal settling velocity for the particle, plotted in a same (Re_u, Fr) space, demonstrating the significance of jet flow on the particle's bouncing motion.

The study on bouncing behaviour of particles settling through a density stratified fluid is clearly still far from comprehensive. For example, it will be of interest to consider a cluster of particles, of which the interactions between particles would lead to more complicated and interesting settling behaviours. Also, particles with irregular shapes can be considered. Both can represent more closely the real situations, such as the aggregation of marine snow.

Acknowledgements

This research has been supported by the National Natural Science Foundation of China (Grant No: 11922212) and the Fundamental Research Funds for the Zhejiang Provincial Universities (Grant No: 2021XZZX017). S.W. gratefully acknowledges the hospitality of the Department of Applied Mathematics and Theoretical Physics, University of Cambridge.

REFERENCES

- ABAID, N., ADALSTEINSSON D. AGYAPONG A. & MCLAUGHLIN, R.M. 2004 An internal splash: Levitation of falling spheres in stratified fluids. *Physics of Fluids* **16** (5), 1567–1580.
- ARDEKANI, A.M. & STOCKER, R. 2010 Stratlets: low reynolds number point-force solutions in a stratified fluid. *Physical review letters* **105** (8), 084502.
- BAYAREH, M., DOOSTMOHAMMADI A. DABIRI S. & ARDEKANI, A.M. 2013 On the rising motion of a drop in stratified fluids. *Physics of Fluids* **25** (10), 023029.
- BLANCHETTE, F. & SHAPIRO, A.M. 2012 Drops settling in sharp stratification with and without marangoni effects. *Physics of Fluids* **24** (4), 042104.
- CAMASSA, R., DING L. MCLAUGHLIN R.M. OVERMAN R. PARKER R. & VAIDYA, A. 2022 Critical density triplets for the arrestment of a sphere falling in a sharply stratified fluid. *arXiv preprint arXiv:2202.09435* .
- CAMASSA, R., FALCON C. LIN J. MCLAUGHLIN R.M. & MYKINS, N. 2010 A first-principle predictive theory for a sphere falling through sharply stratified fluid at low reynolds number. *Journal of Fluid Mechanics* **664**, 436–465.
- CAMASSA, R., FALCON C. LIN J. MCLAUGHLIN R.M. & PARKER, R. 2009 Prolonged residence times for particles settling through stratified miscible fluids in the stokes regime. *Physics of Fluids* **21** (3), 031702.
- DIERCKS, A., ZIERVOGEL K. SIBERT R. JOYE S.B. ASPER V. & MONTROYA, J.P. 2019 Vertical marine snow distribution in the stratified, hypersaline, and anoxic orca basin (gulf of mexico). *Elementa: Science of the Anthropocene* **7**.
- DOOSTMOHAMMADI, A. & ARDEKANI, A.M. 2014a Reorientation of elongated particles at density interfaces. *Physical Review E* **90** (3), 033013.
- DOOSTMOHAMMADI, A., DABIRI S. & ARDEKANI, A.M. 2014b A numerical study of the

- dynamics of a particle settling at moderate reynolds numbers in a linearly stratified fluid. *Journal of Fluid Mechanics* **750**, 5–32.
- EPPE, B.P. 2010 An impulse framework for hydrodynamic force analysis: fish propulsion, water entry of spheres, and marine propellers. PhD thesis, Massachusetts Institute of Technology.
- HANAZAKI, H., KASHIMOTO K. & OKAMURA, T. 2009 Jets generated by a sphere moving vertically in a stratified fluid. *Journal of fluid mechanics* **638**, 173.
- HIGGINSON, R.C., DALZIEL S.B. & LINDEN, P.F. 2003 The drag on a vertically moving grid of bars in a linearly stratified fluid. *Experiments in fluids* **34** (6), 678–686.
- LI, Y., DIDDENS C. PROSPERETTI A. CHONG K.L. ZHANG X. & LOHSE, D. 2019 Bouncing oil droplet in a stratified liquid and its sudden death. *Physical review letters* **122** (15), 154502.
- MAGNAUDET, J. & MERCIER, M.J. 2020 Particles, drops, and bubbles moving across sharp interfaces and stratified layers. *Annual Review of Fluid Mechanics* **52**, 61–91.
- MANDEL, T.L., WALDROP L. THEILLARD M. KLECKNER D. & KHATRI, S. 2020 Retention of rising droplets in density stratification. *Physical Review Fluids* **5** (12), 124803.
- MORDANT, N. & PINTON, J.F. 2000 Velocity measurement of a settling sphere. *The European Physical Journal B-Condensed Matter and Complex Systems* **18** (2), 343–352.
- ORR, T.S., DOMARADZKI J.A. SPEDDING G.R. & CONSTANTINESCU, G.S. 2015 Numerical simulations of the near wake of a sphere moving in a steady, horizontal motion through a linearly stratified fluid at $re = 1000$. *Physics of Fluids* **27** (3), 035113.
- PRAIRIE, J.C. & WHITE, B.L. 2017 A model for thin layer formation by delayed particle settling at sharp density gradients. *Continental Shelf Research* **133**, 37–46.
- SCHLICHTING, H. & KLAUS, J. 2003 *Boundary-layer theory*. Springer Science & Business Media.
- SHARQAWY, M.H., LIENHARD J.H. & ZUBAIR, S.M. 2010 Thermophysical properties of seawater: a review of existing correlations and data. *Desalination and water Treatment* **16** (1-3), 354–380.
- SRDIĆ-MITROVIĆ, A.N., MOHAMED N.A. & FERNANDO, H.J.S. 1999 Gravitational settling of particles through density interfaces. *Journal of Fluid Mechanics* **381**, 175–198.
- TORRES, C. R., HANAZAKI, H., OCHOA, J., CASTILLO, J. & WOERT, M VAN. 2000 Flow past a sphere moving vertically in a stratified diffusive fluid. *Journal of Fluid Mechanics* **417**, 211–236.
- TRUSCOTT, T.T., EPPE B.P. & TECHET, A.H. 2012 Unsteady forces on spheres during free-surface water entry. *Journal of Fluid Mechanics* **704**, 173–210.
- VERSO, L., VAN REEUWIJK M. & LIBERZON, A. 2019 Transient stratification force on particles crossing a density interface. *International Journal of Multiphase Flow* **121**, 103109.
- WELLER, H.G., TABOR G. JASAK H. & FUREBY, C. 1998 A tensorial approach to computational continuum mechanics using object-oriented techniques. *Computers in physics* **12** (6), 620–631.
- WHITE, F.M. & MAJDALANI, J. 2006 *Viscous fluid flow*. New York: McGraw-Hill.
- YICK, K. Y., TORRES, C. R., PEACOCK, T. & STOCKER, R. 2009 Enhanced drag of a sphere settling in a stratified fluid at small reynolds numbers. *Journal of Fluid Mechanics* **632**, 49–68.
- ZHANG, J., MERCIER M.J. & MAGNAUDET, J. 2019 Core mechanisms of drag enhancement on bodies settling in a stratified fluid. *Journal of Fluid Mechanics* **875**, 622–656.